



Tectonic control of erosion in the southern Central Andes



Pedro Val^{a,b,*}, Agostina L. Venerdini^c, William Ouimet^d, Patricia Alvarado^c, Gregory D. Hoke^a

^a 204 Heroy Geology Laboratory, Syracuse University, Syracuse NY, 13244, USA

^b Scripps Institution of Oceanography – Earth Division, University of California, San Diego, La Jolla, CA, 92093, USA

^c CIGEOBIO, Conicet – Dept. Geofísica y Astronomía, Universidad Nacional de San Juan, San Juan, Argentina

^d Dept. of Geography and Center for Integrative Geosciences, University of Connecticut, Storrs, CT, 06269, USA

ARTICLE INFO

Article history:

Received 2 February 2017

Received in revised form 25 September 2017

Accepted 1 November 2017

Available online 7 December 2017

Editor: A. Yin

Keywords:

erosion rate
tectonics
crustal seismicity
precipitation
Andes
landscape evolution

ABSTRACT

Landscape evolution modeling and global compilations of exhumation data indicate that a wetter climate, mainly through orographic rainfall, can govern the spatial distribution of erosion rates and crustal strain across an orogenic wedge. However, detecting this link is not straightforward since these relationships can be modulated by tectonic forcing and/or obscured by heavy-tailed frequencies of catchment discharge. This study combines new and published along-strike average rates of catchment erosion constrained by ¹⁰Be and river-gauge data in the Central Andes between 28°S and 36°S. These data reveal a nearly identical latitudinal pattern in erosion rates on both sides of the range, reaching a maximum of 0.27 mm/a near 34°S. Collectively, data on topographic and fluvial relief, variability of rainfall and discharge, and crustal seismicity suggest that the along-strike pattern of erosion rates in the southern Central Andes is largely independent of climate, but closely relates to the N–S distribution of shallow crustal seismicity and diachronous surface uplift. The consistently high erosion rates on either side of the orogen near 34°S imply that climate plays a secondary role in the mass flux through an orogenic wedge where the perturbation to base level is similar on both sides.

© 2017 Elsevier B.V. All rights reserved.

1. Introduction

Global compilations suggest that climate exerts a significant control on exhumation of rocks in active orogens (e.g. Herman et al., 2013; Yanites and Kesler, 2015). In non-glaciated landscapes, the premise for climatic influence on erosion is straightforward: more precipitation increases river discharge and therefore stream power, which leads to increased rates of fluvial incision (e.g. Ferrier et al., 2013). Moreover, heavy rainfall can lower the threshold hillslope gradient by increasing pore pressure and causing mass-wasting processes and relief reduction (Bookhagen et al., 2005; Gabet et al., 2004; Trauth et al., 2000). In contrast, hyperaridity can bring erosion to a halt and lead to greater surface uplift and topographic growth if tectonic uplift is ongoing (Jordan et al., 2014; Kober et al., 2007). Thus, when mountain ranges grow tall enough to develop orographic precipitation and rain shadows, the climatic patterns can enhance exhumation in the prevailing wind direction and induce an asymmetric mass flux and crustal strain rate, con-

trolling topographic form (e.g. Willett, 1999; Whipple, 2009) and the position of the orogenic thrust front (e.g. Lease et al., 2016; Norton and Schlunegger, 2011).

Despite straightforward predictions by the numerical models (Willett, 1999; Whipple, 2009), explicit field evidence supporting the link between climatically driven erosion and the evolution of mountain ranges has been difficult to consistently identify. The climatic influence on erosion in compressional orogens is often clouded by tectonic deformation because of its control of topographic relief through increased rock and/or surface uplift and the local base level (e.g. Balco et al., 2013; Gasparini and Whipple, 2014; Godard et al., 2014). Also, erosion thresholds and discharge variability will exert a strong influence on the style of erosion and make landscapes less sensitive to increases in runoff (e.g. DiBiase and Whipple, 2011). In these locations, decreasing trends in erosion rates can sometimes be observed in the direction of an increasing precipitation gradient (e.g. Balco et al., 2013; Carretier et al., 2013). Thus, the hypothesis that orographic precipitation in compressional orogens causes greater exhumation needs to be tested in a region where climatic, tectonic, topographic, and erosion rate data are available.

We contribute to this debate by comparing along-strike erosion rates in the Central Andes between 28°S and 36°S, where

* Corresponding author at: Scripps Institution of Oceanography – Earth Division, University of California, San Diego, La Jolla, CA, 92093, USA.

E-mail address: pedroval07@gmail.com (P. Val).

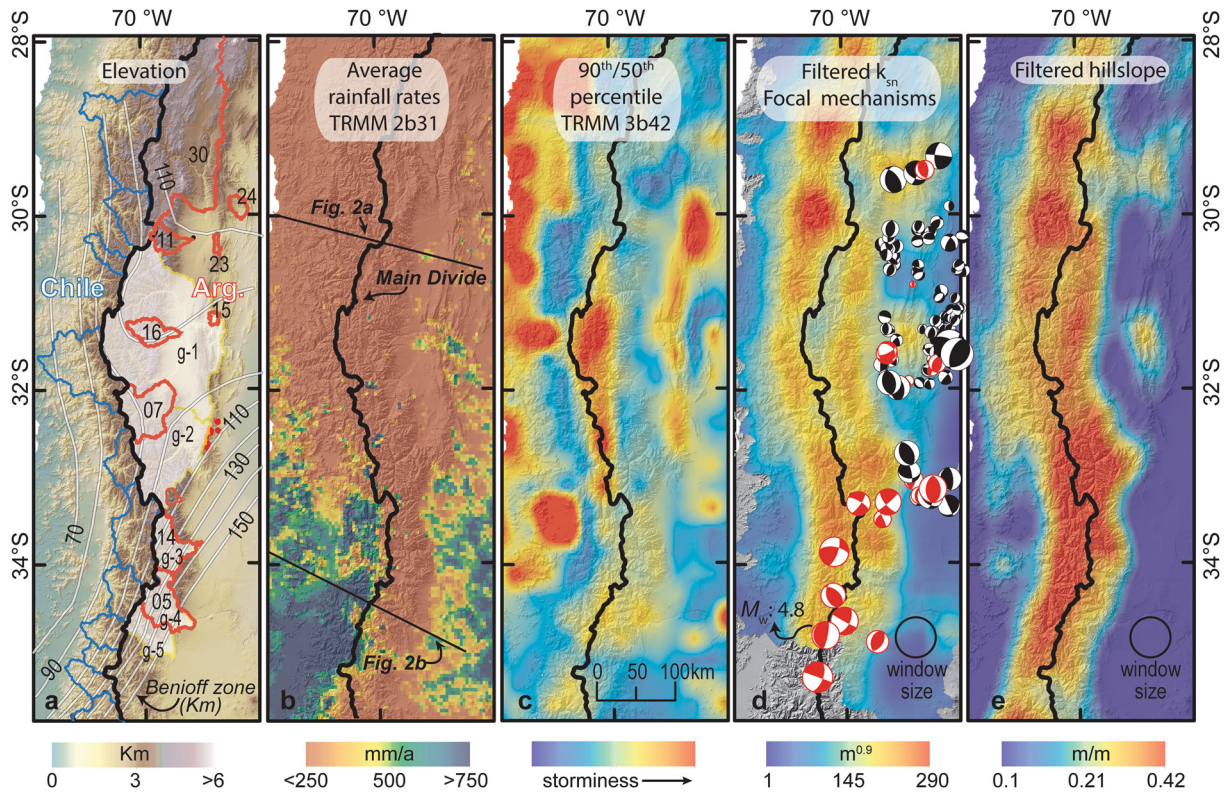


Fig. 1. Southern Central Andes. (a) Topography (SRTM, 90 m). Eastern Andean catchments sampled for CRN are outlined in red; catchments used for gauge data are outlined in yellow with white shading and labeled with the prefix “g”. Western Andean catchments are shown in blue and correspond to Carretier et al. (2013). Depths to Wadati–Benioff zone are shown (white contours) after Anderson et al. (2007). (b) 12-year average precipitation from Tropical Rainfall Measuring Mission (TRMM) after Bookhagen and Strecker (2008). (c) interpolated 90th/50th percentile of daily rainfall using TRMM 3b42 (30 km resolution) from 1998 through 2014 (<http://gcmd.gsfc.nasa.gov>). Higher values reflect heavy-tailed frequency distribution of rainfall rates. (d) Beach ball diagrams showing solutions of compiled and new focal mechanism data (red outline: focal depth <20 km). An earthquake of M_w 4.8 is labeled for scale (see Fig. S1 for solutions outside of map area). Background map: interpolated and filtered fluvial steepness (k_{sn} -normalized steepness index). Discrete k_{sn} values were computed in batch using Stream Profiler (geomorphtools.org) for channels with drainage areas $>50^6$ m², normalized to a reference concavity index of 0.45, and filtered through a 50 km wide low-pass Gaussian moving-window chosen to capture broad, long-wavelength patterns for a qualitative view. (e) Hillslope angles filtered as in d. Note the steepest hillslope and k_{sn} areas between 32°S–34°S. (For interpretation of the references to color in this figure legend, the reader is referred to the web version of this article.)

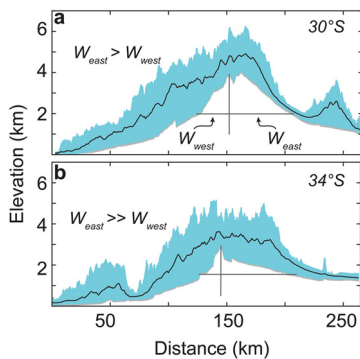


Fig. 2. Elevation swath cross-sections (50 km wide) of the southern Central Andes at 30°S and 34°S (centerlines in Fig. 1b). The shaded region shows the domain between elevation minima and maxima, and the black line shows the mean elevation. The horizontal line shows the half-peak width of the orogen under the drainage divide (vertical line). Note higher asymmetry near 34°S where orographic precipitation is strong (see Fig. 1b).

an orographic rainfall gradient with a three-fold variation in precipitation exists across strike (Fig. 1a, b). This region is ideal to test the predictions of orographic rainfall controls on erosion rates and ultimately orogenic evolution for three main reasons: (1) the mountain range is asymmetric where the orographic effect is strongest (~34°S; Fig. 2); (2) the N–S gradients in curvature, catchment hypsometry, slopes, drainage density, further suggest a climatic influence on topographic form (Carretier et al., 2013;

Rehak et al., 2010); (3) the range of precipitation (<0.25 m/a to >0.75 m/a) and runoff (<0.1 m/a to >0.8 mm/a), are at the transition where landscapes are most sensitive to precipitation and discharge amounts and variability (e.g. DiBiase and Whipple, 2011). Thus, this setting provides a test of the orographic effect hypothesis: erosion rates should be systematically higher in the western Andes south of ~33.5°S (i.e. asymmetric) where it rains 3 to 4 times more than the eastern Andes. In contrast, a tectonic control should reveal symmetric patterns of erosion rates on both sides. From here forward, we refer to the regions east and west of the main drainage divide as eastern and western Andes, respectively (Fig. 1).

In this study, we provide new erosion rate data from the eastern Andes and compile previously published data from both the western and eastern flanks (Carretier et al., 2013; Pepin et al., 2013; Walcek and Hoke, 2012). We pair these data with an assessment of along-strike seismicity, catchment-average topographic and fluvial relief, annual rainfall and runoff, and rainfall and river discharge variability. Our results reveal relationships between erosion rates and hillslope gradient, fluvial relief, and river runoff that have important implications for understanding the evolution of mountain ranges struck by orographic precipitation and rain shadows.

2. The Andes between 28°S and 36°S

Between 28°S and 36°S, the width of the Andes narrows from ~400 km in the Puna plateau to ~250 km south of it, reaching

<150 km south of 33°S (slab angle transition) while maintaining a high mean elevation of ~4 km for at least 6° of latitude despite steep gradients in climate and tectonic shortening (Strecker et al., 2007; Fig. 1a). On the eastern flanks, total shortening, crustal thickness, and Neogene foreland basin infill all decrease southward (Giambiagi et al., 2012; Jordan et al., 2001, 1993), while the total surface uplift since 10 Ma increases (Hoke et al., 2014). The eastern Andean foreland sustains active near-surface deformation at 30°S in the Precordillera (e.g. Allmendinger and Judge, 2014). In contrast, seismic-derived strain rates in the western Andes are the lowest between 28°S and 33°S (Siame et al., 2005). Approximately 2 km of surface uplift occurred in the Pliocene near 34°S in the western Andes (Fariás et al., 2008) based on river profile analysis, which agrees with inferences from the eastern Andes derived from stable isotopes in pedogenic carbonates (Hoke et al., 2014). On the western side, precipitation rates (Fig. 1b) and thicknesses of the preserved trench infill both increase southward (Bangs and Cande, 1997).

The western flank of the Andes at these latitudes exhibit an along-strike pattern of erosion rate that is better correlated with hillslope angles than with its steep precipitation gradient (Fig. 1b; Carretier et al., 2013). Nonetheless, Carretier et al. (2013) attributed a partial control of erosion rate to discharge and rainfall variability (Fig. 1c) and vegetation cover. However, this interpretation is complicated by N–S variations in crustal shortening, thickness, and surface uplift (Giambiagi et al., 2012; Hoke et al., 2014). More importantly, the few existing millennial erosion rate data in the arid to semi-arid parts of the eastern Andes indicate that erosion rates can be similar to, or higher than, those in the western Andes (Nobile et al., 2016; Pepin et al., 2013; Siame et al., 2015; Walcek and Hoke, 2012). This setting is, therefore, an ideal location to investigate spatial patterns of erosion and its implications in the context of a narrow orogenic wedge with variations in climate (e.g. Whipple, 2009).

3. Methods

3.1. Cosmogenic radionuclide and river-gauge erosion rate calculations

We collected nine samples from active, modern river channels in and adjacent to the eastern Andes. Six of these catchments drain the high Andes (Frontal Cordillera and Principal Cordillera) and three drain the Precordillera (Fig. 1; Table 1). Quartz samples were purified at Syracuse University, from which ¹⁰Be was extracted at the University of Pennsylvania following standard methods (von Blanckenburg et al., 1996). ¹⁰Be/⁹Be was measured at the Purdue Rare Isotope Measurement Laboratory and yielded ratios ranging from 16 to 775 × 10⁻¹⁵ with a procedural blank of 1.78 ± 0.27 × 10⁻¹⁵ relative to standards in Nishiizumi et al. (2007) (supplementary data).

¹⁰Be erosion rates were calculated using CRONUS assuming a mean density of 2.7 g/cm³ and scaled for the mean catchment elevation of quartz-contributing lithologies and centroid latitude using the Stone-scaling while accounting for topographic shielding (Balco et al., 2008; Dunne et al., 1999; Schwanghart and Scherler, 2014; Stone, 2000; a table for input in the CRONUS online calculator is provided in the supplementary material). We used the revised sea level high latitude reference ¹⁰Be production rate of 4.1 ± 0.35 at/gyr (Borchers et al., 2016). We selected previously published CRN data from the eastern Andes restricted to the studied transect draining the high Andes and the Precordillera (Pepin et al., 2013; Walcek and Hoke, 2012). Since these studies also used the CRONUS calculator, Stone-scaling routine, and same topographic shielding calculation method, we simply apply a correction factor of 0.91 to the reported erosion rates due to the different sea level high latitude reference production rate used in those studies

Table 1
¹⁰Be results.

Sample ID	Catchment	Lat (°S)	Lon (°W)	Drainage area (km ²)	Granitoid area (%)	Elev. ^a (m)	Hypso. integral ^a	Hillslope gradient ^a (m/m)	k _{sn} ^a (m)	EVI ^a	Precip. ^a (mm/a)	90th/50th	¹⁰ Be (at/g) × 10 ³		Erosion rate (mm/a)		Apparent age (ka)	
													mean	1σ	Mean	1σ (%)		
¹⁰ Be-data																		
PV-14-30	Jáchal	-29.02	-69.37	17954	–	3980	0.46	0.23	260	0.04	55	9	769.9	15.6	0.04	3	8	17
PV-14-24	Huaco	-29.91	-68.72	471	0.8	2070	0.33	0.22	233	0.11	155	13	873	7.3	0.11	8	11	6
PV-14-23	Tranca	-30.34	-69.01	144	0.0	2460	0.48	0.22	314	0.04	142	14	103.5	6.7	0.12	7	10	5
*PV-14-11	Água Negra	-30.29	-69.67	1023	47.0	3930	0.50	0.39	446	0.05	57	9	1030.8	20.1	0.03	0	7	24
PV-14-15	Prec. San Juan	-31.20	-69.04	171	0.0	2320	0.47	0.30	358	0.07	258	10	164.6	5.1	0.07	3	9	9
*PV-14-16	Calingasta	-31.35	-69.88	1410	2.6	3700	0.52	0.41	505	0.05	68	11	427.3	10.0	0.06	2	8	11
A13-07	Los Patos	-32.24	-69.95	3653	30.5	3610	0.36	0.40	418	0.04	144	11	98.7	15.0	0.23	15	17	3
PV-14-14	Tunuyán	-33.80	-69.67	2541	34.0	3580	0.46	0.44	485	0.05	175	10	85.7	3.5	0.28	4	9	2
A13-05	Diamante	-34.47	-69.72	2882	9.1	2890	0.43	0.32	348	0.05	232	11	163.5	6.5	0.10	4	9	6

^aConcentrations might be affected by the contribution of long-lived alluvial fan sediments and were excluded from our analyses.

^a Average computed over the catchment area.

(4.5 at/gyr versus 4.1 at/gyr). The eastern Andean dataset contains catchments that vary in size between 1 to 3000 km², with one reaching 17000 km².

Decadal erosion rates for six eastern Andean catchments were computed from freely available river-gauge data (BDHI, 2017). First, we fit a power-law to sediment and fluvial discharge data which, in most cases, consists of 1–4 observations per month over at least 40 years. We then apply this power-law fit to the complete record of daily discharge to infer the daily sediment load over the full period of observation. The total sediment load divided by the period of observation and catchment area upstream of the gauge station provides the decadal erosion rate. The reported uncertainties correspond to the 1σ of the power-law fit.

3.2. Focal mechanisms

We present 25 compiled (Alvarado et al., 2009, 2005; Alvarado and Beck, 2006; Assumpção and Araujo, 1993; Chiaramonte et al., 2000; Chinn and Isacks, 1983; Ekström et al., 2012) and 99 new focal mechanism solutions for earthquakes in the period of 1944–2014. New data were obtained from the SIEMBRA network, which is composed of 40 broadband seismic stations in the Pampean flat slab (Gans et al., 2011). Focal mechanisms were calculated from least squared error solutions using seismic moment tensor inversion. Earthquake locations were calculated using Hypocenter (Lienert and Havskov, 1995). The analyzed earthquakes range from depths of 46.1 km to 3 km with an average of 27 km (supplementary data). Average magnitude M_w is 3.1 and ranges from 1.3 to 7 (supplementary data).

3.3. Discharge and rainfall variability

River discharge in semi-arid landscapes is more sensitive to temporal variations in rainfall and high-magnitude events are likely necessary to surpass the threshold for geomorphic work (DiBiase and Whipple, 2011; Lague et al., 2005; Molnar et al., 2006). We estimated climatic variability using two different datasets: daily discharge data (BDHI, 2017) and remotely sensed rainfall data (<http://gcmd.gsfc.nasa.gov>). First, we analyzed the variability of discharge in the study area using decadal gauge data when available. Most of the gauge records span at least 40 years (Table 2). A first-order estimation of discharge variability is the cumulative distribution of daily discharge (Q_{daily}) normalized by the long-term mean daily discharge (Q_{mean}), referred to as the dimensionless discharge (Q^* ; DiBiase and Whipple, 2011; Lague et al., 2005). For $Q^* > 1$ (i.e. $Q_{daily} > Q_{mean}$), the slope of the power-law relationship reveals how variable higher-than-average discharge events are (e.g. Lague et al., 2005). The shallower the slope of the distribution over $Q^* > 1$, the more variable. We use a maximum likelihood estimator (MLE) to calculate the slope of this part of the distribution (Clauset et al., 2009) as a proxy for discharge variability in seven catchments along strike between 31°S and 37°S. We calculate the MLE-slope over the range of Q^* that is best described by a power-law, not necessarily all $Q^* > 1$. In this case, the MLE uses a Kolmogorov–Smirnov test to estimate the minimum Q^* and slope that yield the best goodness-of-fit of the power-law (Clauset et al., 2009). It is important to allow the minimum Q^* to vary since it is reflective of the critical discharge to be exceeded for sediment transport and bedrock incision (e.g. Lague et al., 2005), although here it is purely a statistical description of the power-law behavior (Clauset et al., 2009). The commonly reported variability parameter “ k ” in probability density functions of daily discharge is the MLE-slope minus 1.

Second, we analyze rainfall variability using the 90th/50th percentile (i.e. storminess) from 1998 to 2014 using TRMM 3b42 data

Table 2
River-gauge results.

Station	Lat (°S)	Lon (°W)	Drainage area (km ²)	Elev. ^a (m)	Hypso. integral	Hillslope gradient ^b (m/m)	k_{SR} ^a (m)	EVI ^a	Precip. ^a (mm/a)	90th/50th	Runoff (m/a)	Q_{daily} (m ³ /s)		Erosion rate (mm/a)		Period of obs.	MLE Slope-1
												Mean	1σ (%)	Mean	1σ (%)		
San Juan	-31.49	-69.75	13604 ^b	3187	0.38	0.31	317	0.05	71	10	0.77	53.05	0.04	30	1971–2016	2.3 ± 0.1	
La Plateada	-31.85	-69.66	3653	3610	0.36	0.40	418	0.04	144	11	0.362	41.9	0.23 ^c	-	1957–2016	1.4 ± 0.0	
Guido	-32.75	-69.63	7105	3536	0.38	0.41	396	0.04	120	10	0.200	45.1	0.19	30	1956–2016	3.1 ± 0.5	
Tunuyán	-33.80	-69.67	2454	3649	0.46	0.45	485	0.04	175	10	0.360	27.9	0.30	30	1954–2016	4.1 ± 0.1	
La Jaula	-34.47	-69.73	2756	3120	0.43	0.34	348	0.05	232	11	0.380	33.2	0.17	30	1971–2016	4.3 ± 1.3	
Sosneado	-34.82	-69.92	2370	2955	0.37	0.32	283	0.04	322	10	0.511	38.4	0.09	29	1972–2016	5.2 ± 1.6	
Barrancas	-36.49	-70.22	3419	2328	0.36	0.29	290	0.07	-	7	0.330	35.7	0.03	28	1961–2016	5.9 ± 1.8	

^a Average computed over the catchment area.

^b After removing the intermontane-valley, catchment #16, and the Precordillera areas.

^c CRN-derived erosion rate (sediment load data not available).

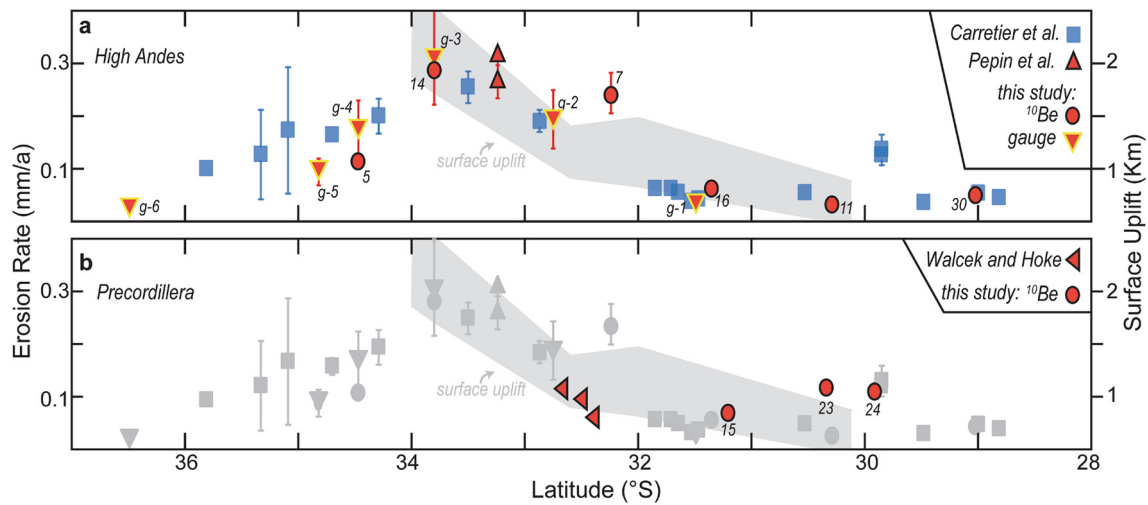


Fig. 3. Erosion rate data from this study and from the literature (Carretier et al., 2013; Pepin et al., 2013; Walcek and Hoke, 2012). Data are separated in catchments draining the high Andes (a) and the Precordillera (b) and in western (blue) and eastern flanks (red). The high Andes data is shown in gray in panel b. Samples #11 and #16 are potentially affected by high-CRN, old alluvial fan deposits. Labels next to the eastern side data correspond to the respective catchments in Fig. 1a. The gray envelope depicts total surface uplift since 10 Ma after Hoke et al. (2014) and is limited by the reported upper and lower 1σ standard deviations. (For interpretation of the references to color in this figure legend, the reader is referred to the web version of this article.)

interpolated over the study area, which serves as a proxy for discharge variability in the absence of river-gauge data. The original dataset has 30 km resolution (<http://gcmd.gsfc.nasa.gov>). While this coarser dataset misses important features such as orographic precipitation (e.g. Castino et al., 2016), it provides a high temporal resolution that accurately captures rainfall variability (Boers et al., 2016).

3.4. Catchment-wide parameters

The average erosion rates are commonly compared to other catchment-average parameters to tease out individual contributions that may be linked to climate or tectonics. In this study, we computed catchment-averages of hillslope gradient, normalized fluvial steepness index (k_{sn}), hypsometric integral, elevation, precipitation, storminess, and enhanced vegetation index (EVI). Topographic parameters were computed from the 90 m resolution Shuttle Radar Topographic Mission digital elevation model (Farr et al., 2007). Local hillslope gradient was computed for a nine cell neighborhood and averaged over the entire catchment area. k_{sn} , which is the local fluvial slope normalized by the contributing drainage area raised to a reference concavity index (in this case, -0.5), was computed for individual stream segments with a minimum contributing upstream area of 8 km² using TopoToolbox and averaged over the catchment area (Schwanghart and Scherler, 2014). EVI was obtained from the MODIS MOD13Q1 dataset for the period of 2000–2016 (lpdaac.usgs.gov).

We use the 5 km-resolution Tropical Rainfall Measurement Mission (TRMM) 2b31 precipitation dataset to compute the 12-year mean catchment precipitation rates (Bookhagen and Strecker, 2008). While this dataset only integrates from 1998 to 2009, its annual precipitation amounts and spatial patterns, including the southern Central Andes rain shadow, agree (i.e. RMSE < 0.03) with the gridded rain-gauge data from the Global Precipitation Climatology Centre, which integrates over 50 years (1951–2000) with a resolution of ~ 30 km (Bookhagen and Strecker, 2008; Schneider et al., 2017). Twelve years is obviously short compared to the integration times of ¹⁰Be erosion rates from this study. However, while precipitation amounts may have varied over millennial timescales, the overall spatial precipitation patterns are likely the same since the Pleistocene based on equilibrium line altitude observations and marine core records (Clapperton, 1994;

Haselton et al., 2002; Lamy et al., 2001). Furthermore, arid conditions in the eastern flanks of the southern Central Andes were in place at least since the late Miocene (Strecker et al., 2007). For the reasons outlined, we assume the spatial patterns of precipitation used in this study are representative of longer timescales, but the absolute precipitation rates probably varied.

3.5. Nonlinear hillslope erosion model

We follow the routine described in Ouimet et al. (2009) and fit a nonlinear hillslope-erosion model (Roering et al., 2001) to the erosion rate and hillslope data. According to this model, which assumes steady state ($dz/dt = 0$), the 1-D form of a hillslope is:

$$z(x) = \frac{-S_c^2}{2\beta\varepsilon} \left[\sqrt{K^2 + (2\beta\varepsilon/S_c)^2} - K \ln \left(\frac{\sqrt{K^2 + (2\beta\varepsilon/S_c)^2} + K}{2\beta\varepsilon/S_c} \right) \right] \quad (1)$$

where z is elevation (L), x distance (L), S_c the critical hillslope (L/L), β the ratio of rock to sediment densities (assumed ~ 1.3), ε the erosion rate (L/T), and K a transport efficiency coefficient (L^2/T). The mean equilibrium gradient (S_μ) over the characteristic hillslope length (L_H), that is, from the hilltop to the hillslope-channel transition; is therefore:

$$S_\mu = \frac{z(0) - z(L_H)}{L_H} \quad (2)$$

Given these two equations, we seek the combination of K and S_c for a given L_H that best describes the observed dataset of S and ε . Our inspection of satellite images and river profile data shows that a plausible range of L_H is between 200 and 800 m. We report K and S_c values for L_H between 200 and 500 m.

4. Results

4.1. Erosion rates

The new ¹⁰Be erosion rates range from ~ 0.04 to ~ 0.27 mm/a and, assuming steady state, integrate between 25 ka and 2 ka, respectively. ¹⁰Be erosion rates in the high eastern Andes range from low values of 0.04–0.07 mm/a in the northern basins (29°S) to the

Southern Central Andean basins			
	Western	Eastern	All
Drainage Area	-0.30	0.08	0.07
Elevation	-0.01	0.04	-0.05
Hypsometric Integral	-0.11	-0.11	-0.10
Hillslope Gradient	0.70	0.89	0.76
Norm. Steepness index (k_{sn})	0.28	0.92	0.66
Enhanced Vegetation Index	-0.23	0.23	0.20
Precipitation	0.66	-0.10	0.32
Runoff	0.44	0.27	0.28
Q-Variability parameter	0.54	-0.40	0.43
90 th /50 th Percentile	-0.33	-0.36	-0.40


Correlation with erosion rate (R): -1  1

Fig. 4. Correlation coefficients (R) between basin-average ¹⁰Be-erosion rate and other parameters separated by western (Carretier et al., 2013) and eastern (this study; Walcek and Hoke, 2012; Pepin et al., 2013) basins and the complete dataset. Erosion rates were regressed as log-transforms (except for runoff and Q-variability). R values for hillslope angle and k_{sn} correspond to the nonlinear fits from Fig. 3 calculated for each dataset separately.

highest observed from 0.15 to 0.27 mm/a between 32°S and 34°S (Fig. 3a). Catchments draining the tectonically active Precordillera erode between 0.08 and 0.13 mm/a, similar to those observed by Walcek and Hoke (2012) (Fig. 3b). Decadal erosion rates in the eastern Andes vary between 0.02 and 0.3 mm/a and follow the same latitudinal pattern as the ¹⁰Be erosion rates (Tables 1, 2; Fig. 3). One outlier in this pattern is the San Juan catchment (g-1 in Fig. 1a). Here, the decadal erosion rate is 0.03 mm/a while other subcatchments within it show ¹⁰Be erosion rates of 0.07 mm/a (Precordillera thrust-top) and 0.23 mm/a (Los Patos catchment – 07 in Fig. 3; see Table 1).

The most important observation is that the along strike pattern and magnitude of erosion rates are similar in the eastern and western flanks despite contrasts in precipitation (Fig. 3). South of 34°S, both millennial and decadal erosion rates in the eastern and western flanks decrease (Fig. 3). However, contrary to the areas north of 34°S, the southward decrease in erosion rates is less pronounced in the western flank. North of 34°S, catchments draining the eastern Andes have either similar or higher erosion rates than those in the western side (Carretier et al., 2013) (Fig. 3). These rates are at the lower end of the observed long-term average for the Central Precordillera, which is >0.2 mm/a based on (U-Th-Sm)/He thermochronology (Fosdick et al., 2015). Correlations with catchment-average topographic and climatic parameters are summarized in Fig. 4 and described separately below.

4.2. Hillslope gradient, fluvial steepness, and erosion rates

We observe a positive correlation between erosion rates, fluvial steepness and hillslope gradient (Fig. 5). Erosion rates increase nonlinearly with hillslope gradient and are well described by the 1-D hillslope erosion/transport model ($R^2 = 0.8$; Roering et al., 2001). The correlation reveals a low critical hillslope gradient (S_c) of 0.46 m/m (~25° hillslope angle) and a transport coefficient (K) of 0.008–0.02 m²/a (for L_H between 200 and 500 m) in the eastern flanks, compared to 0.53 m/m (~28° hillslope angle) and K of 0.004–0.02 m²/a (recalculated here) in the western flanks (Carretier et al., 2013). This relationship remains significant after including other semi-arid mountainous catchments in the flanks of the Altiplano–Puna plateaus to the NE ($R^2 = 0.77$, not shown; Bookhagen and Strecker, 2012). The millennial erosion rates are also well correlated with the catchment average normalized fluvial steepness index (k_{sn}) by a power law ($R^2 = 0.84$, Fig. 5).

4.3. Runoff and decadal erosion rates

The bulk of the observations described below come from the dataset in the western Andes (Carretier et al., 2013). The erosion rate observations from the eastern Andes fall within the same runoff-erosion rate trends observed by Carretier et al. (2013) in the western Andes (Fig. 6). Runoff in the western side can be twice as high as the eastern side over the same latitudes (e.g. 33.8°S and ~35°S) and increase southward to ~2.5 m/a (Fig. 6a; Carretier et al., 2013). This 1.5 to 2-fold increase in runoff across strike is not translated into an increase in erosion rates (Fig. 6a, b–e). This is because the highest observed erosion rates correspond to runoff rates of 0.4 m/a (Fig. 6b). Since erosion rates vary the most for hillslopes steeper than 0.3 m/m (Fig. 5), we separated the erosion rate-runoff data into three broadly defined hillslope gradient bins: <0.3, 0.3–0.4, and >0.4 m/m (Fig. 6b–e). Where hillslope gradients exceed 0.4 m/m, erosion rates (decadal and millennial) reach maximum values of ~0.3 mm/a on both sides of the Andes at a runoff of 0.37 m/a, after which erosion rates are insensitive to runoff (Fig. 6c). Similarly, decadal erosion rates range from 0.05 to ~0.17 mm/a between 36°S and 34°S for hillslope gradients between 0.3 and 0.4 m/m while runoff varies between 0.3 m/a in the eastern side and >1.2 m/a in the western side (Figs. 5, 6) and, again, are highest near a runoff rate of ~0.38 m/a (Fig. 6d). Lastly, for slopes shallower than 0.3 m/m, decadal erosion rates continue to rise with increasing runoff up to 2.2 m/a (Fig. 5e). Thus, for the steepest catchments (mean gradients > 0.3 m/m), erosional efficiency seems to occur at 0.38 m/a runoff. When mean catchment

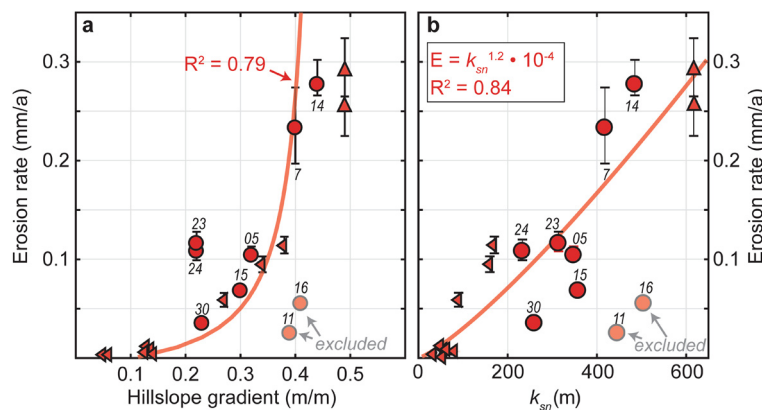


Fig. 5. (a) Nonlinear relationship between ¹⁰Be erosion rates and mean hillslope gradient fit by the 1-D hillslope model (Roering et al., 2001) for the eastern Andes using data from this study and the literature (Pepin et al., 2013; Walcek and Hoke, 2012). Data points follow the notation used in Fig. 3. Samples #11 and #16 are clear outliers potentially due to contribution from high-CRN alluvial surfaces and were not used in the regression; (b) Positive correlation between catchment-average k_{sn} and ¹⁰Be erosion rates. Data for this plot are provided in Tables 1 and S1.

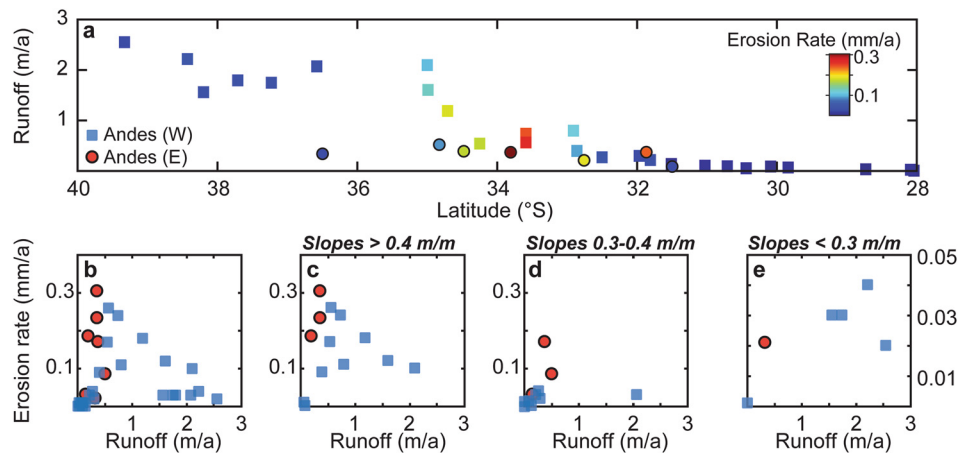


Fig. 6. Latitudinal changes and relationships between runoff and decadal erosion rates. (a) Along-strike variations in runoff separated by basins in the western (squares, Carretier et al., 2013) and eastern Andes (circles, this study) and colored by erosion rate; (b) Trade-offs between erosion rate and runoff separated in western (blue squares) and eastern (red circles) as labeled in panel “a”; (c–e) Same as panel “b” but separated in three hillslope gradient groups (>0.4, 0.3–0.4, and <0.3 m/m). Note the change in the y-axis’ interval in panel “e”. Note the anti-correlation between runoff and erosion rates in the western Andes (Carretier et al., 2013). (For interpretation of the references to color in this figure legend, the reader is referred to the web version of this article.)

slopes are <0.3 m/m, erosional efficiency is potentially highest at runoff rates greater than 1 m/a.

Because of the relationships described above, erosion rates end up having an overall weak dependency on runoff over both flanks of the mountain range ($R = 0.28$; Fig. 4). However, until the highest erosional efficiency is reached, they do in fact correlate positively (Carretier et al., 2013). Also, because precipitation increases southward in the western flanks, the relationship with erosion rates is similar ($R = 0.66$; Fig. 4). Since the range in precipitation rates is small in the eastern flanks, the correlation with erosion rates is poor ($R = -0.1$; Fig. 4). Taken together, erosion rates in the Central Andes between 28°S and 36°S only weakly correlate with precipitation ($R = 0.32$; Fig. 4).

4.4. Discharge and rainfall variability

The cumulative distributions of discharge in eastern Andean catchments between 31°S and 37°S are remarkably similar for $Q^* < 2.5$ in all seven catchments (Fig. 7a). For $Q^* > 2.5$, there is a northward increase in variability as indicated by progressively shallower slopes of the cumulative distributions (Fig. 7; Table 2). As implicit in the distributions for $Q^* < 2.5$, average daily discharge does not vary dramatically over the eastern catchments (Figs. 6–7; Table 2), nor does runoff (Fig. 6a). Furthermore, the average discharge on the eastern flanks is not offset by discharge variability and the latter is very weakly correlated with erosion rates (Fig. 4). In contrast, the range of discharge variability is much greater in the western flanks (Fig. 7b; Carretier et al., 2013). There, discharge variability is also weakly, but positively correlated with erosion rates (Fig. 4). Combined, the correlation between discharge variability and erosion rates on both sides of the mountain range is weak (Fig. 4).

The 90th/50th percentile of rainfall rates implies a stormier nature north of 32°S (Fig. 1c), consistent with the discharge data on the western (Carretier et al., 2013) and eastern sides. We also observe higher rainfall variability along the western Andes between 28°S and 32°S (Fig. 1c), consistent with the greater discharge variability there (Carretier et al., 2013). Over the eastern Andes, we observe a narrow band of higher rainfall variability along the high Andes between 30°S and 33°S and along some parts of the Western and Central Cordillera at 30°S (Fig. 1c), which potentially contributes to the discharge variability observed in the gauge data (Fig. 7). However, the 90th/50th percentile data do not reveal the

systematically stormier nature from 37°S to 31°S that is evident in the discharge data.

4.5. Earthquake depth, magnitude, and distribution

North of 33°S, earthquakes are concentrated along the western and eastern Precordillera ranges with an average depth of 26.45 km and M_w magnitudes ranging from 1.3 to 7 (Fig. 1d; supplementary data). South of 33°S, earthquakes retreat to the high Andes, are mostly of magnitude M_w 5 or higher and average ~16 km depth (Fig. 1d; supplementary data). The changes in earthquake focal depth, mechanism, and hypocenter coincide with changes in the long-wavelength hillslope gradient, fluvial steepness index, and catchment-average erosion rate (Figs. 1d, 3). They also coincide with changes in the angle of the subducting Nazca plate from flat to normal between 32°S and 33.5°S (Fig. 1a).

5. Discussion

5.1. Minor climatic control of catchment-average erosion rates

In general, for a given average catchment hillslope gradient, co-variations in erosion rates and runoff are potentially controlled by the relationship between discharge variability and runoff (i.e. DiBiase and Whipple, 2011). Our study demonstrates that, over this segment of the Andes (excluding the Precordillera), neither rainfall amount, storminess, or discharge variability exert a primary influence on the average discharge nor ^{10}Be or decadal erosion rates (Fig. 4). More importantly, we show that discharge variability exerts a stronger control over erosion in catchments with shallower slopes due to the higher critical discharge necessary to initiate sediment transport and bedrock incision (e.g. DiBiase and Whipple, 2011; Lague, 2014; Lague et al., 2005). Since decadal erosion rates in the study area are insensitive to runoff > ~0.4 m/a for hillslope gradients steeper than 0.3 m/m, most erosional work is done at average flow conditions in the eastern side and below average flow conditions in the western side south of ~31°S (Fig. 5a). Given that decadal and millennial erosion rates are similar and the correlations with runoff also hold for the millennial rates (e.g. Carretier et al., 2013), it is likely that the millennial erosion rates in the eastern side follow the same relationship with average runoff. Thus, where hillslopes are steeper than 0.3 m/m, low-frequency high-discharge events such as those caused by southern climatic oscillations are less important and erosion rates (millennial and decadal) appear to

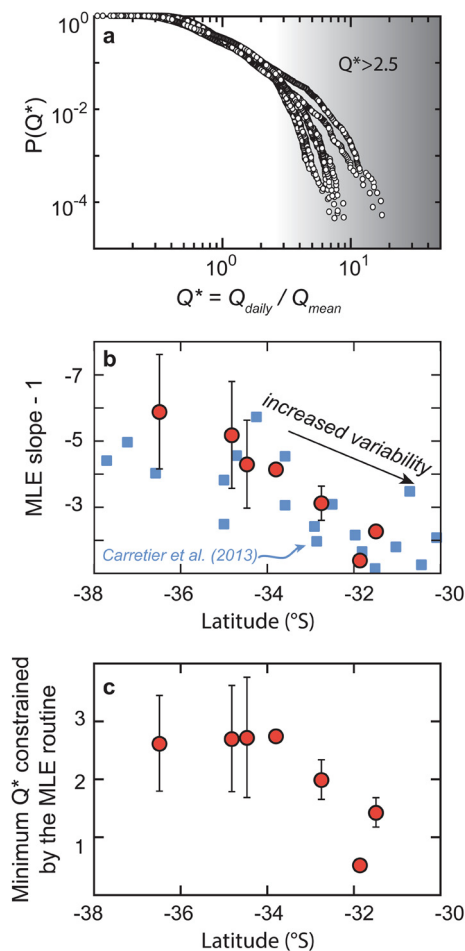


Fig. 7. (a) Daily discharge (Q_{daily}) variability for seven catchments in Argentina shown as a cumulative distribution function of Q_{daily} normalized by the average daily discharge over the entire period (Q_{mean}). Most catchments contain at least 44 years of daily averages. The number of observations vary between 13103 (San Juan River, g-1 in Fig. 1a) and 22700 (Tunuyán River, g-3 in Fig. 1a). Note that the catchments analyzed here have a similar cumulative distribution of daily discharge for $Q^* < 2.5$; (b) Maximum likelihood estimation (MLE) of the variability parameter (MLE-slope - 1) of the power-law distributions shown in panel “a” calculated over best-fit minimum Q^* values determined via KS test (panel c). For reference, equivalent variability values from the western Andes are shown in blue (Carretier et al., 2013); (c) Minimum Q^* constrained by the MLE routine. Daily discharge data are provided as supplementary material. (For interpretation of the references to color in this figure legend, the reader is referred to the web version of this article.)

be well-approximated by the stream power assumptions (DiBiase and Whipple, 2011; Lague et al., 2005). This is consistent with the observation that average flow conditions are not offset by climatic variability given that the slopes of the cumulative distributions only differ for $Q^* > 2.5$ along-strike in the eastern side (Fig. 7a; see also Molnar et al., 2006).

Interestingly, the little influence of climatic variability on discharge in this region is potentially a function of discharge being buffered by glacial meltwater, which in turn is only weakly affected by southern climatic oscillations (Masiokas et al., 2006). Nonetheless, climatic oscillations clearly influence high discharge events, which is consistent with observations from other regions in northwest Argentina (e.g. Castino et al., 2016). Again, because erosion is efficient at average runoff, the infrequent extremes are less important when it comes to erosion.

Since peak erosional efficiency seems to depend on the average catchment hillslope gradients along strike (Fig. 6b–e), erosion rates will be similar on both sides as long as the average catchment hillslope gradients are equivalent across-strike and average

annual runoff near or above the threshold for sediment transport and bedrock incision. Thus, the 1.5 to 2-fold increase in runoff and the minimum 3-fold increase in precipitation across strike (orographic effect) is unlikely to contribute to mass flux out of the mountain range where hillslope gradients are > 0.3 m/m, which encompasses the region between 28°S and 36°S . This interpretation is reinforced by the similar pattern of erosion rates on both sides of the mountain range revealed in this study (Fig. 3). Other southward trends, such as increasing frequency of glaciers and decreasing equilibrium line altitude (e.g. Rehak et al., 2010), and increasing vegetation cover (Carretier et al., 2013) are inconsistent with the simultaneous southward decrease in erosion rates on both sides.

Because of low hillslope gradients, the low erosion rates ($\sim 0.02 \pm 0.01$ mm/a) south of 36°S in the eastern Andes are possibly influenced by the rain shadow. That erosion rates continue to increase from runoffs of 0.3 m/a (east) to ~ 1 m/a (west) suggests that the average runoff in the eastern Andes is below that required for peak erosional efficiency (Fig. 6e), although the number of basins falling in this category is small. This suggests that the wetter climate in the western Andes may drive more erosion compared to the eastern Andes in the same latitude. Nonetheless, erosion rates for these shallower hillslope gradients in the western side suggest that 0.04 mm/a is the maximum over these latitudes. Thus, even at peak erosional efficiency, climatic oscillations nor rainfall could cause the general southward decrease in erosion rates observed on both sides.

The consistency of ^{10}Be erosion rates between 0.06 and 0.12 mm/a in the unglaciated Precordillera (30°S – 32.5°S) demonstrates that rivers maintain their erosive power despite aridity. This is intriguing because, unlike the high Andes catchments, runoff rates strongly depend on rainfall because discharge is not maintained by glacial meltwater. Interestingly, ^{10}Be erosion rates are mostly < 0.05 mm/a in the western Andes (Carretier et al., 2013) over similarly dry regions but less seismically active in the upper crust (Fig. 1d; Siame et al., 2005; Alvarado et al., 2007). This observation suggests that seismic activity modulates erosion rates in this region (see also Siame et al., 2015). The weaker dependence of erosion rates on fluvial steepness in the western flanks can be partly attributed to two catchments in the northern arid areas with high rock strength granitoids that promote steeper hillslope gradients but lower erosion rates (see Carretier et al., 2013).

Lastly, if CRN concentrations reflected glacial contribution of low ^{10}Be sediments or were biased by glacial shielding of bedrock, the relationship of mean catchment hillslope gradient, fluvial steepness, and erosion rates would be weak or non-existent. Moreover, the southward decrease in ELA would promote greater shielding in the southern regions and bias ^{10}Be concentrations towards low values, which is opposite to what we observe. This would be especially visible on the western Andes where last glacial maximum equilibrium line altitudes were hundreds of meters lower than in the eastern Andes (Clapperton, 1994), but this is not likely the case in the western flanks either (e.g. Carretier et al., 2013).

5.2. Pronounced orogenic influence

The observed patterns of erosion, seismicity, and crustal shortening vary consistently with changes in the angle of the subducting Nazca plate from north to south (Fig. 1a). At first, their general spatial coincidence suggests they are linked during mountain range evolution. However, the growth of topography in the high Andes is diachronous along strike and likely independent of the slab angle (Giambiagi et al., 2012; Hoke et al., 2014).

The observed erosion rates observed in the southern Central Andes more likely reflect the history of mountain building and orogenesis; most specifically, its tectonic activity (seismicity), sur-

face and rock uplift, shortening, and crustal thickness. North of 32°S, crustal shortening is mostly accommodated in the Argentine Precordillera from the middle Miocene to present (Allmendinger and Judge, 2014; Jordan et al., 2001; Levina et al., 2014) where crustal seismicity is high and erosion rates are >0.08 mm/a despite arid conditions (Fig. 1d). Moreover, the retro-arc Precordillera and Sierras Pampeanas mountain ranges (east of the high Andes) between 29°S and 32°S experience erosion rates in excess of 0.1 mm/a at least since the late Miocene (Amidon et al., 2017; Fosdick et al., 2015; Jordan et al., 2001; Siame et al., 2015; Val et al., 2016; Walcek and Hoke, 2012), which is evidence of much greater mass removal compared to the western forearc flanks (Carretier et al., 2013). In contrast, seismicity is low and erosion rates are <0.05 mm/a in the high Andes over these same latitudes (Figs. 1d, 3a). Here, little surface uplift has occurred near the high Andes since the late Miocene (Hoke et al., 2014). To the south (>33°S), the coincidence of higher surface uplift in the Pliocene (Fariás et al., 2008; Hoke et al., 2014) is consistent with focused seismicity under the high Andes as well as high erosion rates (>0.2 mm/a) on both sides of the range (Fig. 1d–f). Here, movement along strike-slip and reverse faults at shallow depths not only indicate the potential for base level perturbation, but might also lead to increased slope instability and mass wasting events (e.g. Antinao and Gosse, 2009). Overall, the strong N–S gradient in surface uplift and loci of recorded earthquakes coincide with the observed higher erosion rates in the eastern Andes north of 32°S and the similarity between millennial erosion rates on both sides south of 32°S (Fig. 3). Taken together, these observations reveal that active rock uplift exerts a first order control on erosion rates via the combined effects of base level change, steepened hillslopes, both of which contribute to obscuring the effects of the rain shadow.

Since erosion rates on both sides of the high Andes mimic the north to south increase in surface uplift until 34°S (Fig. 3), it seems plausible to assume a southward decrease in surface uplift south of 34°S that is similar to the erosion rate pattern. This is consistent with inferences of structural uplift data, which are highest near 34°S and steadily decrease until 34.7°S, albeit with high uncertainties (Giambiagi et al., 2012). However, erosion rates on the western flanks decrease less abruptly than in the eastern flanks (Fig. 2). For example, from 33.8°S to 34.4°S they decrease from 0.24 mm/a to between 0.15–0.19 mm/a on the western flanks (~–0.08 to –0.15 mm/a per latitudinal degree) versus 0.27 mm/a to 0.1 mm/a on the eastern flanks (~–0.28 mm/a per latitudinal degree). Perhaps this is related to higher precipitation and runoff on the western flanks sustaining higher erosion rates compared to the eastern flanks. Yet, the average hillslope gradient also follows a similar pattern with an abrupt step south of 34°S on the eastern flanks compared to a gradual decrease on the western flanks (Fig. 1e). Thus, as the hillslope gradients may influence erosional efficiency (Fig. 6), the discrepancy in erosion rates over these latitudes is likely a function of hillslope gradient and secondarily a function of the lower runoff rates on the eastern sides.

5.3. Implications for orogenic wedge evolution

Surface uplift near 34°S started some time since 5 Ma (Hoke et al., 2014; Fariás et al., 2008), implying a minimum surface uplift rate of 0.4 mm/a, which is slightly higher than the millennial-scale erosion rates in this area. That these rates are similar suggests that the pattern of erosion observed here partly corresponds to an ongoing and/or delayed erosional response to this earlier change in fluvial relief (e.g. Val et al., 2016). This suggests that the patterns we observe in this study may reflect long-term processes over timescales relevant to orogenic wedge evolution as discussed below.

In theory, symmetrical or asymmetrical mass-flux through an orogenic wedge depends on subduction-driven accretion and the spatial distribution of erosional efficiency on the surface, which can be regulated by climate (e.g. Willett, 1999). Given the observed spatial distribution of precipitation, numerical models of orogenic-wedges would predict higher exhumation on the western side of the Andes south of 33°S (Whipple, 2009; Willett, 1999). The Central Andes between 28 and 36°S clearly do not follow these predictions (Fig. 3). Instead, the similar along-strike pattern and magnitude of decadal and millennial erosion rates on both sides between 33°S and 36°S suggests that mass flux out of the orogen, specifically the high Andes, has been symmetric about the divide and, in some cases, higher in the dry side (i.e. Precordillera), over the 2–6 ka integration time of ¹⁰Be erosion rates (Table 1). Our results imply that once fluvial relief and hillslope gradients are enhanced by tectonic uplift, the effects of orographic precipitation, rain shadows, and climate variability become less important if the average runoff is enough for high erosional efficiency. This is the case in the study area due to a combination of steep hillslope gradients, river steepness, and peak erosional efficiency near average runoff rates, which are sustained by glacial meltwater from the high Andes. Even without glacial meltwater, high erosion rates could still be maintained as is the case in the non-glaciated Precordillera fold-and-thrust belt. Thus, our results imply that compressional orogens with rain shadows not necessarily develop asymmetric exhumation and the erosional response is most sensitive to perturbations to base level.

6. Conclusions

We presented new millennial and decadal erosion rates on the eastern flanks of the Central Andes between 28°S and 36°S, which we compared with other published millennial rates from the western flanks. The observed decadal and millennial erosion rates on both sides of the Andes are similar along strike despite variations in precipitation and runoff (Fig. 1b, Fig. 3). The runoff rate responsible for maximum erosional efficiency seems to depend on average hillslope gradient and is attained around the average runoff rate for most of the catchments in the eastern flanks, which in turn reduces the importance of discharge variability. Erosion rates correlate well with topographic parameters, which are best explained by the timing and gradient of along-strike surface uplift and with the spatial pattern of crustal seismicity. These results suggest that the spatial patterns of erosion need not correlate with the prevailing wind direction in orogens affected by orographic precipitation. The average mass flux out of the orogenic wedge may still be symmetric about the divide despite the presence of a rain shadow.

Acknowledgements

This study was partially funded by the American Chemical Society Petroleum Research Fund (award 52480-DNI08 to G. Hoke), by Syracuse University's College of Arts and Sciences and Department of Earth Sciences. P. Val was supported by a CAPES/Science Without Borders doctoral fellowship (#0515-12-4) from the Brazilian government. We thank Devin McPhillips for samples and a constructive review of an earlier version of this manuscript, an anonymous reviewer also for a constructive review that helped improve this manuscript, Jane Willenbring for insightful discussions, Rafael Hernán and Rachel Valletta for field and laboratory support, respectively.

Appendix A. Supplementary material

Supplementary material related to this article can be found online at <https://doi.org/10.1016/j.epsl.2017.11.004>. These data in-

clude the Google map of the most important areas described in this article.

References

- Allmendinger, R.W., Judge, P.A., 2014. The Argentine Precordillera: a foreland thrust belt proximal to the subducted plate. *Geosphere* 10, 1203–1218. <https://doi.org/10.1130/GES01062.1>.
- Alvarado, P., Barrientos, S., Saez, M., Astroza, M., Beck, S., 2009. Source study and tectonic implications of the historic 1958 Las Melosas crustal earthquake, Chile, compared to earthquake damage. *Phys. Earth Planet. Inter.* 175, 26–36. <https://doi.org/10.1016/j.pepi.2008.03.015>.
- Alvarado, P., Beck, S., 2006. Source characterization of the San Juan (Argentina) crustal earthquakes of 15 January 1944 (Mw 7.0) and 11 June 1952 (Mw 6.8). *Earth Planet. Sci. Lett.* 243, 615–631. <https://doi.org/10.1016/j.epsl.2006.01.015>.
- Alvarado, P., Beck, S., Zandt, G., 2007. Crustal structure of the south-central Andes Cordillera and backarc region from regional waveform modelling. *Geophys. J. Int.* 170, 858–875. <https://doi.org/10.1111/j.1365-246X.2007.03452.x>.
- Alvarado, P., Beck, S., Zandt, G., Araujo, M., Triep, E., 2005. Crustal deformation in the south-central Andes backarc terranes as viewed from regional broadband seismic waveform modelling. *Geophys. J. Int.* 163, 580–598. <https://doi.org/10.1111/j.1365-246X.2005.02759.x>.
- Amidon, W.H., Fisher, G.B., Burbank, D.W., Ciccio, P.L., Alonso, R.N., Gorin, A.L., Silverhart, P.H., Kylander-clark, A.R.C., Christoffersen, M.S., 2017. Mio-Pliocene aridity in the south-central Andes associated with Southern Hemisphere cold periods. *Proc. Natl. Acad. Sci.* 114 (25), 6474–6479. <https://doi.org/10.1073/pnas.1700327114>.
- Anderson, M., Alvarado, P., Zandt, G., Beck, S., 2007. Geometry and brittle deformation of the subducting Nazca Plate, Central Chile and Argentina. *Geophys. J. Int.* 171, 419–434. <https://doi.org/10.1111/j.1365-246X.2007.03483.x>.
- Antinao, J.L., Gosse, J., 2009. Large rockslides in the Southern Central Andes of Chile (32–34.5°S): tectonic control and significance for Quaternary landscape evolution. *Geomorphology* 104, 117–133. <https://doi.org/10.1016/j.geomorph.2008.08.008>.
- Assumpção, M., Araujo, M., 1993. Effect of the Altiplano–Puna plateau, South America, on the regional intraplate stresses. *Tectonophysics* 221, 475–496. [https://doi.org/10.1016/0040-1951\(93\)90174-I](https://doi.org/10.1016/0040-1951(93)90174-I).
- Balco, G., Finnegan, N., Gendaszek, A., Stone, J.O.H., Thompson, A., 2013. Erosional response to northward-propagating crustal thickening in the coastal ranges of the U.S. Pacific Northwest. *Am. J. Sci.* 313, 790–806. <https://doi.org/10.2475/11.2013.01>.
- Balco, G., Stone, J.O., Lifton, N.A., Dunai, T.J., 2008. A complete and easily accessible means of calculating surface exposure ages or erosion rates from ¹⁰Be and ²⁶Al measurements. *Quat. Geochronol.* 3, 174–195. <https://doi.org/10.1016/j.quageo.2007.12.001>.
- Bangs, N.L., Cande, S.C., 1997. Episodic development of a convergent margin inferred from structures and processes along the southern Chile margin. *Tectonics* 16, 489. <https://doi.org/10.1029/97TC00494>.
- BDHI, 2017. Base de Datos Hidrológica Integrada. <http://bdhi.hidricosargentina.gov.ar>.
- Boers, N., Bookhagen, B., Marwan, N., Kurths, J., 2016. Spatiotemporal characteristics and synchronization of extreme rainfall in South America with focus on the Andes Mountain range. *Clim. Dyn.* 46, 601–617. <https://doi.org/10.1007/s00382-015-2601-6>.
- Bookhagen, B., Strecker, M.R., 2008. Orographic barriers, high-resolution TRMM rainfall, and relief variations along the eastern Andes. *Geophys. Res. Lett.* 35, L06403. <https://doi.org/10.1029/2007GL032011>.
- Bookhagen, B., Strecker, M.R., 2012. Spatiotemporal trends in erosion rates across a pronounced rainfall gradient: examples from the southern Central Andes. *Earth Planet. Sci. Lett.* 327–328, 97–110. <https://doi.org/10.1016/j.epsl.2012.02.005>.
- Bookhagen, B., Thiede, R.C., Strecker, M.R., 2005. Late Quaternary intensified monsoon phases control landscape evolution in the northwest Himalaya. *Geology* 33, 149–152. <https://doi.org/10.1130/G20982.1>.
- Borchers, B., Marrero, S., Balco, G., Caffee, M., Goehring, B., Lifton, N., Nishiizumi, K., Phillips, F., Schaefer, J., Stone, J., 2016. Geological calibration of spallation production rates in the cronus-earth project. *Quat. Geochronol.* 31, 188–198. <https://doi.org/10.1016/j.quageo.2015.01.009>.
- Carretier, S., Regard, V., Vassallo, R., Aguilar, G., Martinod, J., Riquelme, R., Pepin, E., Charrier, R., Hérail, G., Farías, M., Guyot, J.-L., Vargas, G., Lagane, C., 2013. Slope and climate variability control of erosion in the Andes of central Chile. *Geology* 41, 195–198. <https://doi.org/10.1130/G33735.1>.
- Castino, F., Bookhagen, B., Strecker, M.R., 2016. Rainfall variability and trends of the past six decades (1950–2014) in the subtropical NW Argentine Andes. *Clim. Dyn.* 48, 1–19. <https://doi.org/10.1007/s00382-016-3127-2>.
- Chiaramonte, L., Ramos, V.A., Araujo, M., 2000. Estructura y sismotectónica del anticlinal Barrancas, Cuenca Cuyana, provincia de Mendoza. *Rev. Asoc. Geol. Argent.* 55.
- Chinn, D.S., Isacks, B.L., 1983. Accurate source depths and focal mechanisms of shallow earthquakes in western South America and in the New Hebrides Island Arc. *Tectonics* 2, 529–563.
- Clapperton, C.M., 1994. The quaternary glaciation of Chile: a review. *Rev. Chil. Hist. Nat.* 67, 369–383.
- Clauset, A., Shalizi, C.R., Newman, M.E., 2009. Power-law distributions in empirical data. *SIAM Rev.* 51.
- DiBiase, R.A., Whipple, K.X., 2011. The influence of erosion thresholds and runoff variability on the relationships among topography, climate, and erosion rate. *J. Geophys. Res., Earth Surf.* 116, 1–17. <https://doi.org/10.1029/2011JF002095>.
- Dunne, J., Elmore, D., Muzikar, P., 1999. Scaling factors for the rates of production of cosmogenic nuclides for geometric shielding and attenuation at depth on sloped surfaces. *Geomorphology* 27, 3–11. [https://doi.org/10.1016/S0169-555X\(98\)00086-5](https://doi.org/10.1016/S0169-555X(98)00086-5).
- Ekström, G., Nettles, M., Dziewoński, A.M., 2012. The global CMT project 2004–2010: centroid-moment tensors for 13,017 earthquakes. *Phys. Earth Planet. Inter.* 200–201, 1–9. <https://doi.org/10.1016/j.pepi.2012.04.002>.
- Farías, M., Charrier, R., Carretier, S., Martinod, J., Fock, A., Campbell, D., Cáceres, J., Comte, D., 2008. Late Miocene high and rapid surface uplift and its erosional response in the Andes of central Chile (33°–35°S). *Tectonics* 27, 767–788. <https://doi.org/10.1029/2006TC002046>.
- Farr, T.G., Rosen, P.A., Caro, E., Crippen, R., Duren, R., Hensley, S., Kobrick, M., Paller, M., Rodriguez, E., Roth, L., Seal, D., Shaffer, S., Shimada, J., Umland, J., Werner, M., Oskin, M., Burbank, D., Alsdorf, D., 2007. The shuttle radar topography mission. *Rev. Geophys.* 45, 1–33. <https://doi.org/10.1029/2005RG000183>.
- Ferrier, K.L., Huppert, K.L., Perron, T., 2013. Climatic control of bedrock river incision. *Nature* 496, 206–211. <https://doi.org/10.1038/nature11982>.
- Fosdick, J.C., Carrapa, B., Ortíz, G., 2015. Faulting and erosion in the Argentine Precordillera during changes in subduction regime: reconciling bedrock cooling and detrital records. *Earth Planet. Sci. Lett.* 432, 73–83. <https://doi.org/10.1016/j.epsl.2015.09.041>.
- Gabet, E.J., Pratt-Sitaula, B.A., Burbank, D.W., 2004. Climatic controls on hillslope angle and relief in the Himalayas. *Geology* 32, 629–632. <https://doi.org/10.1130/G20641.1>.
- Gans, C.R., Beck, S.L., Zandt, G., Gilbert, H., Alvarado, P., Anderson, M., Linkimer, L., 2011. Continental and oceanic crustal structure of the Pampean flat slab region, western Argentina, using receiver function analysis: new high-resolution results. *Geophys. J. Int.* 186, 45–58. <https://doi.org/10.1111/j.1365-246X.2011.05023.x>.
- Gasparini, N.M., Whipple, K.X., 2014. Diagnosing climatic and tectonic controls on topography: eastern flank of the northern Bolivian Andes. *Lithosphere* 6, 230–250. <https://doi.org/10.1130/L322.1>.
- Giambiagi, L., Mescua, J., Bechis, F., Tassara, A., Hoke, G., 2012. Thrust belts of the southern Central Andes: along-strike variations in shortening, topography, crustal geometry, and denudation. *Bull. Geol. Soc. Am.* 124, 1339–1351. <https://doi.org/10.1130/B30609.1>.
- Godard, V., Bourlès, D.L., Spinabella, F., Burbank, D.W., Bookhagen, B., Fisher, G.B., Moulin, A., Léanni, L., 2014. Dominance of tectonics over climate in Himalayan denudation. *Geology* 42, 243–246. <https://doi.org/10.1130/G35342.1>.
- Haselton, K., Hilley, G., Strecker, M.R., 2002. Average Pleistocene climatic patterns in the southern Central Andes: controls on mountain glaciation and paleoclimate implications. *J. Geol.* 110, 211–226. <https://doi.org/10.1086/338414>.
- Herman, F., Seward, D., Valla, P.G., Carter, A., Kohn, B., Willett, S.D., Ehlers, T.A., 2013. Worldwide acceleration of mountain erosion under a cooling climate. *Nature* 504, 423–426. <https://doi.org/10.1038/nature12877>.
- Hoke, G.D., Giambiagi, L.B., Garzone, C.N., Mahoney, J.B., Strecker, M.R., 2014. Neogene paleoelevation of intermontane basins in a narrow, compressional mountain range, southern Central Andes of Argentina. *Earth Planet. Sci. Lett.* 406, 153–164. <https://doi.org/10.1016/j.epsl.2014.08.032>.
- Jordan, T.E., Allmendinger, R.W., Damanti, J.F., Drake, R.E., 1993. Chronology of motion in a complete thrust belt: the Precordillera, 30–31°S, Andes Mountains. *J. Geol.* 101, 135–156.
- Jordan, T.E., Kirk-Lawlor, N.E., Blanco, N.P., Rech, J.A., Cosentino, N., 2014. Landscape modification in response to repeated onset of hyperarid paleoclimate states since 14 Ma, Atacama Desert, Chile. *Geol. Soc. Am. Bull.* 126, 1016–1046. <https://doi.org/10.1130/B30978.1>.
- Jordan, T.E., Schlunegger, F., Cardozo, N., 2001. Unsteady and spatially variable evolution of the Neogene Andean Bermejo foreland basin, Argentina. *J. South Am. Earth Sci.* 14, 775–798. [https://doi.org/10.1016/S0895-9811\(01\)00072-4](https://doi.org/10.1016/S0895-9811(01)00072-4).
- Kober, F., Ivy-Ochs, S., Schlunegger, F., Baur, H., Kubik, P.W., Wieler, R., 2007. Denudation rates and a topography-driven rainfall threshold in northern Chile: multiple cosmogenic nuclide data and sediment yield budgets. *Geomorphology* 83, 97–120. <https://doi.org/10.1016/j.geomorph.2006.06.029>.
- Lague, D., 2014. The stream power river incision model: evidence, theory and beyond. *Earth Surf. Process. Landf.* 39, 38–61. <https://doi.org/10.1002/esp.3462>.
- Lague, D., Hovius, N., Davy, P., 2005. Discharge, discharge variability, and the bedrock channel profile. *J. Geophys. Res., Earth Surf.* 110. <https://doi.org/10.1029/2004JF000259>.
- Lamy, F., Hebbeln, D., Röhl, U., Wefer, G., 2001. Holocene rainfall variability in southern Chile: a marine record of latitudinal shifts of the Southern Westerlies. *Earth Planet. Sci. Lett.* 185, 369–382. [https://doi.org/10.1016/S0012-821X\(00\)00381-2](https://doi.org/10.1016/S0012-821X(00)00381-2).
- Lease, R.O., Ehlers, T.A., Enkelmann, E., 2016. Large along-strike variations in the onset of Subandean exhumation: implications for Central Andean orogenic growth. *Earth Planet. Sci. Lett.* 451, 62–76. <https://doi.org/10.1016/j.epsl.2016.07.004>.

- Levina, M., Horton, B.K., Fuentes, F., Stockli, D.F., 2014. Cenozoic sedimentation and exhumation of the foreland basin system preserved in the Precordillera thrust belt (31–32°S), southern central Andes, Argentina. *Tectonics* 33, 1659–1680. <https://doi.org/10.1002/2013TC003424>.
- Lienert, B.R., Havskov, J., 1995. A computer program for locating earthquakes both locally and globally. *Seismol. Res. Lett.* 66, 26–36. <https://doi.org/10.1785/gssrl.66.5.26>.
- Masiokas, M.H., Villalba, R., Luckman, B.H., Le Quesne, C., Aravena, J.C., 2006. Snowpack variations in the Central Andes of Argentina and Chile, 1951–2005: large-scale atmospheric influences and implications for water resources in the region. *J. Climate* 19, 6334–6352. <https://doi.org/10.1175/JCLI3969.1>.
- Molnar, P., Anderson, R.S., Kier, G., Rose, J., 2006. Relationships among probability distributions of stream discharges in floods, climate, bed load transport, and river incision. *J. Geophys. Res., Earth Surf.* 111, 1–10. <https://doi.org/10.1029/2005JF00310>.
- Nishizumi, K., Imamura, M., Caffee, M.W., Southon, J.R., Finkel, R.C., McAninch, J., 2007. Absolute calibration of ¹⁰Be AMS standards. *Nucl. Instrum. Methods Phys. Res., Sect. B, Beam Interact. Mater. Atoms* 258, 403–413. <https://doi.org/10.1016/j.nimb.2007.01.297>.
- NóBILE, J.C., Martini, M.A., Dávila, F.M., 2016. Cosmogenic ¹⁰Be denudation rates and geomorphometric analysis in the Ambato range (28°–29°S), Sierras Pampeanas, Argentina. *Quat. Int.*, 1–12. <https://doi.org/10.1016/j.quaint.2016.01.009>.
- Norton, K., Schlunegger, F., 2011. Migrating deformation in the Central Andes from enhanced orographic rainfall. *Nat. Commun.* 2, 584. <https://doi.org/10.1038/ncomms1590>.
- Ouimet, W.B., Whipple, K.X., Granger, D.E., 2009. Beyond threshold hillslopes: channel adjustment to base-level fall in tectonically active mountain ranges. *Geology* 37, 579–582. <https://doi.org/10.1130/G30013A.1>.
- Pepin, E., Carretier, S., Héral, G., Regard, V., Charrier, R., Farías, M., García, V., Giambiagi, L., 2013. Pleistocene landscape entrenchment: a geomorphological mountain to foreland field case, the Las Tunas system, Argentina. *Basin Res.* 25, 613–637. <https://doi.org/10.1111/bre.12019>.
- Rehak, K., Bookhagen, B., Strecker, M.R., Echtler, H.P., 2010. The topographic imprint of a transient climate episode: the western Andean flank between 15–5° and 41–5°S. *Earth Surf. Process. Landf.* 35, 1516–1534. <https://doi.org/10.1002/esp.1992>.
- Roering, J.J., Kirchner, J.W., Dietrich, W.E., 2001. Hillslope evolution by nonlinear, slope-dependent transport: steady state morphology and equilibrium adjustment timescales. *J. Geophys. Res.* 106, 2053. <https://doi.org/10.1029/2001JB000323>.
- Schneider, U., Finger, P., Meyer-christoffer, A., Rustemeier, E., Ziese, M., Becker, A., 2017. Evaluating the hydrological cycle over land using the newly-corrected precipitation climatology from the Global Precipitation Climatology Centre (GPCP). *Atmosphere (Basel)* 8. <https://doi.org/10.3390/atmos8030052>.
- Schwanghart, W., Scherler, D., 2014. Short Communication: TopoToolbox 2 – MATLAB-based software for topographic analysis and modeling in Earth surface sciences. *Earth Surf. Dyn.* 2, 1–7. <https://doi.org/10.5194/esurf-2-1-2014>.
- Siame, L.L., Bellier, O., Sébrier, M., Araujo, M., 2005. Deformation partitioning in flat subduction setting: case of the Andean foreland of western Argentina (28°S–33°S). *Tectonics* 24, 1–24. <https://doi.org/10.1029/2005TC001787>.
- Siame, L.L., Sébrier, M., Bellier, O., Bourlès, D., Costa, C., Ahumada, E.A., Gardini, C.E., Cisneros, H., 2015. Active basement uplift of Sierra Pie de Palo (Northwestern Argentina): rates and inception from ¹⁰Be cosmogenic nuclide concentrations. *Tectonics* 34, 1129–1153. <https://doi.org/10.1002/2014TC003771>.
- Stone, J.O., 2000. Air pressure and cosmogenic isotope production. *J. Geophys. Res.* 105, 23,753–23,759.
- Strecker, M.R., Alonso, R.N., Bookhagen, B., Carrapa, B., Hilley, G.E., Sobel, E.R., Trauth, M.H., 2007. Tectonics and climate of the Southern Central Andes. *Annu. Rev. Earth Planet. Sci.* 35, 747–787. <https://doi.org/10.1146/annurev.earth.35.031306.140158>.
- Trauth, M.H., Alonso, R.A., Haselton, K.R., Hermanns, R.L., Strecker, M.R., 2000. Climate change and mass movements in the NW Argentine Andes. *Earth Planet. Sci. Lett.* 179, 243–256. [https://doi.org/10.1016/S0012-821X\(00\)00127-8](https://doi.org/10.1016/S0012-821X(00)00127-8).
- Val, P., Hoke, G.D., Fosdick, J.C., Wittmann, H., 2016. Reconciling tectonic shortening, sedimentation and spatial patterns of erosion from ¹⁰Be paleo-erosion rates in the Argentine Precordillera. *Earth Planet. Sci. Lett.* 450, 173–185. <https://doi.org/10.1016/j.epsl.2016.06.015>.
- von Blanckenburg, F., Belshaw, N.S., O’Nions, R.K., 1996. Separation of ⁹Be and cosmogenic ¹⁰Be from environmental materials and SIMS isotope dilution analysis. *Chem. Geol.* 129, 93–99. [https://doi.org/10.1016/0009-2541\(95\)00157-3](https://doi.org/10.1016/0009-2541(95)00157-3).
- Walcek, A.A., Hoke, G.D., 2012. Surface uplift and erosion of the southernmost Argentine Precordillera. *Geomorphology* 153–154, 156–168. <https://doi.org/10.1016/j.geomorph.2012.02.021>.
- Whipple, K.X., 2009. The influence of climate on the tectonic evolution of mountain belts. *Nat. Geosci.* 2, 97–104. <https://doi.org/10.1038/ngeo413>.
- Willet, S.D., 1999. Orogeny and orography: the effects of erosion on the structure of mountain belts. *J. Geophys. Res.* 104, 28957–28981.
- Yanites, B.J., Kesler, S.E., 2015. A climate signal in exhumation patterns revealed by porphyry copper deposits. *Nat. Geosci.* 8. <https://doi.org/10.1038/ngeo2429>.